

Assessing and Validating the Crash Behavior of Securalex[®]HS, a High-Strength Crashworthy Aluminum Alloy, Using the GISSMO Model

Callum J. Corbett, Laurent Laszczyk, Olivier Rebuffet
Constellium Technology Center, CS10027, Voreppe 38410, France

Abstract

Specialized aluminum alloys play an ever increasing role in today's automotive industry. The desire for lightweighting is driven by both performance aspects as well as the legislative framework regarding emissions and fuel efficiency. Using aluminum rolled products for structural car body parts requires good formability and high mechanical properties paired with predictable and safe performance under crash loading.

Simulating and predicting the crash behavior requires a detailed material model including damage and failure. To this extent, a vast range of experiments are performed on Securalex[®]HS samples. The relevant state of the material is the in-service temper, so that a heat treatment is applied to all samples prior to testing. In order to compare the simulation results to the experiments, digital image correlation techniques are used to measure strains on the specimen surfaces during testing.

After calibrating the plastic material response, a detailed failure model is required. Using the GISSMO model, an equivalent plastic strain to failure curve depending on stress triaxiality is defined. It is parametrized with three variables and coupled with an optimizer based on the simplex method. By defining suitable error functions based on the simulation results, it is possible to optimize the failure curve and obtain a good correlation with the experiments. The final step lies in validating the failure model. To this end, the calibrated model is used to simulate and predict the deformation and crack initiation during the quasi-static axial crush of a square profile. The results are compared to experiments done on two-piece friction-stir welded boxes.

Introduction

Vehicle safety is not only a regulatory requirement but also a quality criterion and selling point. Increasing the passive safety of a car while reducing its weight leads to a conflict of interest. In order to provide a high level of safety while reducing weight and optimizing use of resources, a simulation-driven development is unavoidable.

To use highly specialized aluminum alloys like Securalex[®]HS for structural components, a detailed damage and fracture model is required for the development process. To obtain a model that can be calibrated in a reasonable amount of time and depends on a limited number of parameters, only the most relevant effects are taken into account. In addition, the computational cost of the model should remain manageable to avoid excessive runtimes since the model is aimed at component and full vehicle crash simulations. For this purpose, the model targets shell elements with an edge length of around 4mm.

In the following, the material in question is presented and the GISSMO damage model implemented in LS-DYNA[®] is summarized briefly together with the Hosford-Coulomb model which is used to parametrize the strain to failure curve. Three short sections are dedicated to constitutive modeling, the experiments performed for failure calibration and the finite element models used. Identification of the failure parameters and the validation of the model using a friction stir welded box structure under axial compressive loading is discussed, followed by the transfer of the model from solid elements to shell elements. A summary and outlook concludes this paper.

Material

The material of interest in this study is the aluminum product Securalex[®]HS. This product is part of the 6-serie and was developed specifically to provide an enhanced compromise between high strength and crash ductility. The appropriate in-service temper to reach such performances is over-aged (T7). To this end, a post-forming heat treatment has to be introduced such that the manufacturing route for such components is: stamping in solutionized temper (T4), heat treatment in a batch furnace, assembly. The mechanical properties in the T4 and T7 temper are summarized in Tab. 1.

	YS [MPa]	UTS [MPa]	Uniform elongation [%]
T4	125	230	20
T7	270	290	10

Tab. 1: Typical mechanical properties of the Securalex[®]HS in the as-delivered (T4) and in-service (T7) temper.

In the following study, the material tested is Securalex[®]HS at temper T7 and thickness 2.5mm. Regarding the work hardening performed during forming, trials show that the time and temperature of the heat treatment are sufficient to obtain fully recovered material in T7 temper. The pre-damaging that may have taken place during forming is neglected.

GISSMO and Hosford-Coulomb Model

To model damage and fracture of the material, the GISSMO model is chosen. It is a stress-state dependent, phenomenological damage model which is highly flexible. By means of the *ADD_EROSION material card it can be added to arbitrary material models and is thus independent of the choice of constitutive model.

Damage is accumulated incrementally in each time step depending on the current equivalent plastic strain increment $\Delta\varepsilon_{pl}$, an equivalent plastic strain to failure ε_f , the damage exponent φ , and the current damage value D according to

$$\Delta D = \frac{\varphi D^{(1-\frac{1}{\varphi})}}{\varepsilon_f} \Delta\varepsilon_{pl} \quad (1)$$

where the damage variable is initialized to $D = 10^{-20}$. It is possible to define the equivalent plastic strain to failure as a function of stress triaxiality and the Lode angle parameter in the GISSMO model. However, in the scope of sheet metal like it is considered in this work the assumption of plane stress can be made, such that the stress state can be characterized by the just the stress triaxiality η , see [1]. The stress triaxiality is defined as

$$\eta = \frac{\sigma_h}{\sigma_{eq}} \quad (2)$$

with the hydrostatic stress σ_h and the equivalent von Mises stress σ_{eq} .

The equivalent plastic strain to failure then only depends on the triaxiality, $\varepsilon_f = \varepsilon_f(\eta)$. It is input as tabulated data, however the curve is defined analytically according to the Hosford-Coulomb model [2]

$$\varepsilon_f(\eta) = b(1 + c)^{\frac{1}{n}} \left(\left[\frac{1}{2} ((f_1 - f_2)^a + (f_2 - f_3)^a + (f_1 - f_3)^a) \right]^{\frac{1}{a}} + c(2\eta + f_1 + f_3) \right)^{\frac{1}{n}} \quad (3)$$

parametrized by a , b , and c . The functions f_i depend on the Lode angle for general stress states but can be expressed as functions of triaxiality in the case of plane stress. For practical purposes the parameter n can be set to 0.1 rather than deriving it from the consistent transformation from the stress to strain space, leaving only three parameters to fit.

Parameter b corresponds to the failure strain under constant uniaxial or biaxial tensile loading with a triaxiality of $\eta = 1/3$ and $\eta = 2/3$, respectively. Parameter c mainly governs the shape of the failure curve in the region $\eta < 1/3$ while parameter a influences the overall shape. This is illustrated in Fig. 1 where b is fixed to 1 and the other two parameters vary. On the left-hand side c is fixed to 0.05 while a varies, while on the right-hand side a is fixed to 1.5 while c varies. Reasonable ranges for the parameters are $a \in [1, 2]$ and $c \in [0, 0.1]$, which also includes the special case of a constant failure strain $\varepsilon_f(\eta) = b$ for $a = 2$ and $c = 0$.

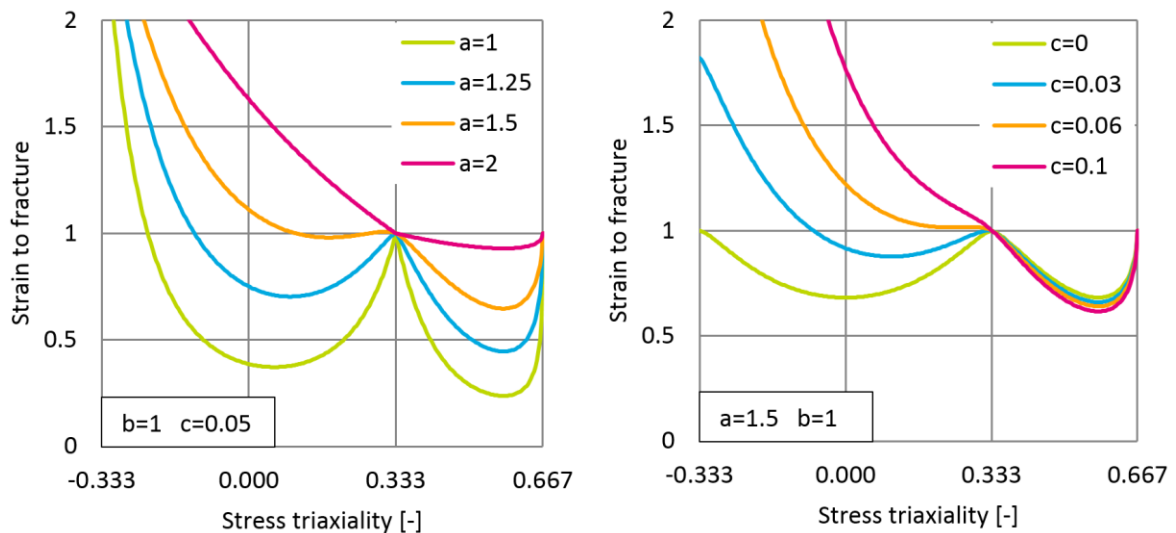


Fig. 1: Parametrized failure strain curve for $b = 1$. On the left-hand side c is fixed to 0.05 and on the right-hand side a is fixed to 1.5 while the other variable is varied.

Constitutive Modeling

In order to calibrate the material model numerous experiments are performed. First, standard tensile tests are used to obtain the elastic material properties and calibrate the hardening curve, shown in Fig. 2.

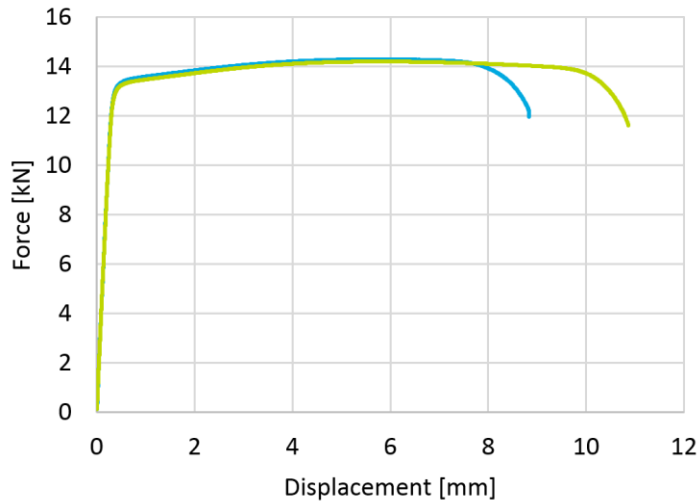


Fig. 2: Force-displacement curves of tensile tests in rolling direction

Additionally, tensile tests are performed in 0°, 30°, 45°, 60°, and 90° direction with respect to the rolling direction in order to assess the anisotropy of the material. Due to the low anisotropic effects, the isotropic material model *MAT_024 is chosen despite its restriction to von Mises plasticity.

Identification of the flow curve can be done with the experimental data up until the point of necking. The extrapolation of the flow curves is adjusted using simulations in order to fit the post-necking behavior up to fracture. Considering the true stress and true plastic strain that can be extracted from the tensile test data, two analytical hardening models are fit to the data independently. The Swift hardening law

$$\sigma_S = K(\epsilon_0 + \epsilon_{pl})^n \tag{4}$$

on the one hand and a Voce-type hardening law

$$\sigma_V = B - (B - A) \exp(-m \epsilon_{pl}) \tag{5}$$

on the other hand. Both models are able to represent the test data well within the valid region until the onset of necking. While the exponential Voce-type model saturates at high strain values, the Swift model which is a power law shows further hardening, as can be seen in Fig. 3.

The proposed model for hardening is a linear combination of the Swift and Voce models above. Introducing a parameter α and keeping the analytically fit parameters constant, the combined hardening behavior

$$\sigma(\alpha) = \alpha \sigma_V + (1 - \alpha) \sigma_S \tag{6}$$

can be defined as a function of one variable. For $\alpha = 1$ this results in the Voce model and for $\alpha = 0$ in the Swift model. An example for $\alpha = 0.5$ is shown in Fig. 2.

Using a tapered tensile test, the parameter α defining the post-necking behavior is fit by reverse engineering. The area between the force-displacement curves of the experiment and the simulation is taken as a measure for the error. This corresponds to a difference in energy which is

minimized in an iterative procedure to simulate the material behavior beyond necking accurately. The finite

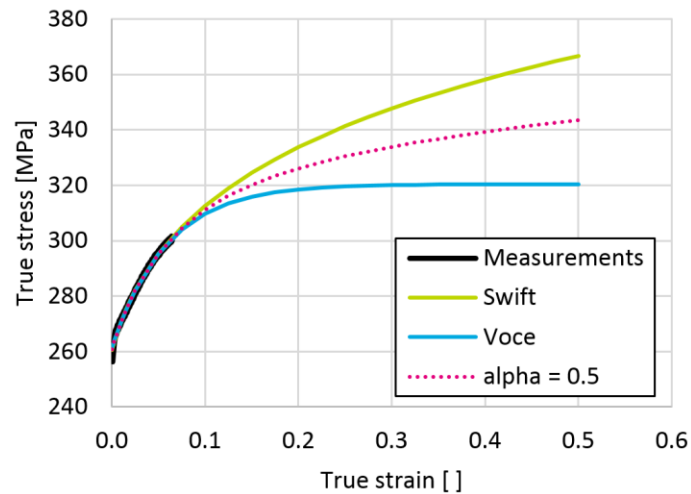


Fig. 3: Fit of hardening models to experimental data

element mesh used for the optimization has an element edge length of 0.1mm in the calibrated zone in order to eliminate mesh size effects. The parameters of the Swift and Voce model derived analytically and the linear combination parameter obtained as the result an optimization procedure are summarized in Tab. 2.

Swift mode parameters			Voce model parameters			Combination
K	ϵ_0	n	A	B	m	α
393.9	0.024	0.111	261.3	320.4	17.15	0.1

Tab. 2: Parameters of the combined Swift-Voce model given by Eq. 6.

Experiments for Failure Calibration

In order to calibrate a stress-state dependent failure model, multiple experiments leading to failure under different load cases must be considered. In addition, digital image correlation (DIC) is used to observe the strain field on the surface of the samples during testing. This allows for a correlation not only of force and displacement, but also the strain field between experiments and simulation.

The four sample geometries used for the calibration are depicted in Fig. 4 during and after testing. On the left the equivalent strain post-processed with the DIC measurement data is shown as overlay on each sample, while the right shows the samples after failure. The speckle pattern applied to the calibrated zone is required for the DIC measurement.

Finite Element Models for Failure Calibration

The width of the calibrated zone is 5.0mm for the tensile tests and 4.0mm and 6.5mm for the 0° and 45° shear samples, depicted in Fig. 4. Considering the thickness of 2.5mm it is clear that the plane stress assumption is not valid for these samples.

For this reason, volumetric models are used for calibration of the failure model and the results later transferred to shell elements. An element edge length of 0.1mm is used in the calibrated zone

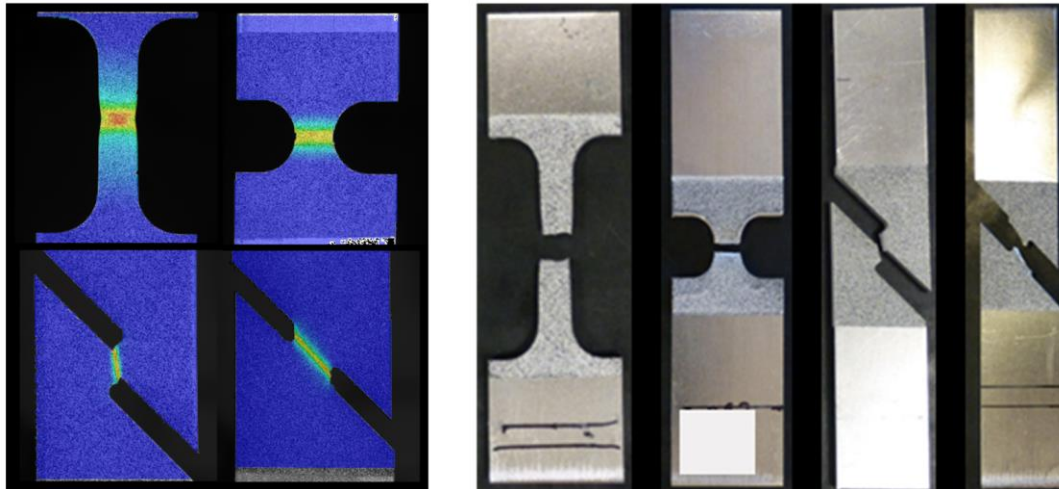


Fig. 4: Sample geometries for failure calibration during and after testing with DIC

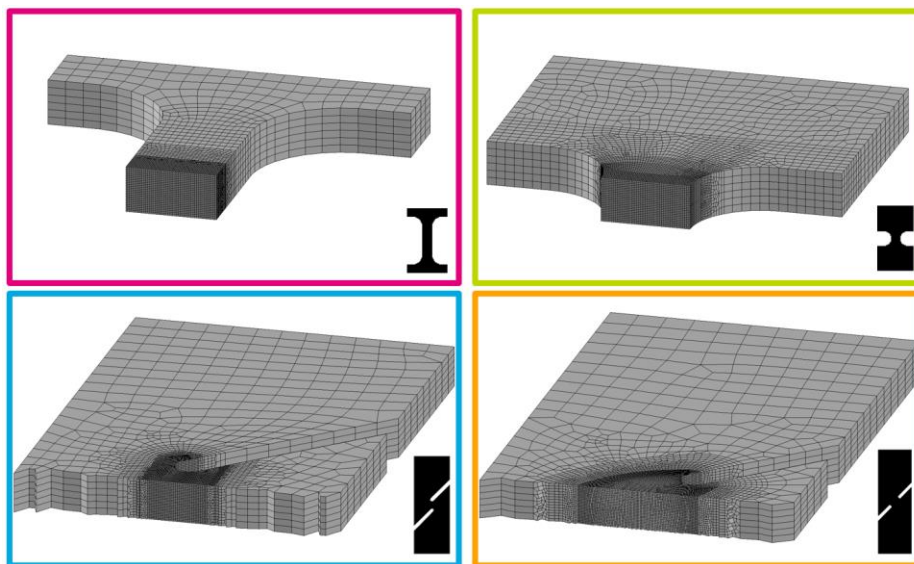


Fig. 5: Cut through the FE models used for failure calibration. The element edge length is 0.1mm in the calibrated zone.

order to capture the behavior accurately. A cut through the meshes is depicted in Fig. 5. For the tensile samples, three symmetry planes can be exploited, while only one can be used for the shear samples.

Failure Parameter Identification

Using Eq. 3 to describe the failure curve there are three parameters to identify: a , b , and c . For the tensile test, the triaxiality is initially $1/3$ but increases before failure due to necking. The final strain value of such a specimen can however be used as an initial guess for the parameter b . Reasonable initial guesses for parameters a and c can be found by running computations without a failure model and observing the evolution of triaxiality and equivalent plastic strain of a critical element until the point of failure in the experiment.

An iterative optimization procedure is run to determine the three parameters. However, the choice of a suitable objective function is not trivial. Using the difference in energy by comparing the force-displacement curves of simulation and experiment is chosen as measure for the error. For each sample the error is calculated individually and the sum of the normalized errors is taken as global objective function. By normalizing the data it is ensured that each sample contributes equally to the global objective function. The strain values measured via DIC are used in a second step to validate the results but are not included in the objective function for simplicity. Once the sample is entirely fractured, the force-displacement curve of the simulation exhibits large oscillations. Due to this, it should be truncated beforehand. Different choices for the truncation are possible, for example at the first negative force value, after a drop in force of a given magnitude, or dependent on the number of deleted elements. The latter option is considered here.

Let n_f be the total number of failed elements in the simulation, after which the sample is completely separated. A reasonable comparison can then be done up until the time when $n \in [1, n_f]$ elements have failed. For $n = 1$ the force-displacement curves are compared until the first element fails, for $n = n_f$ until the samples are completely separated.

Since the GISSMO model only describes crack initiation and does not include crack propagation, the choice of $n = 1$ seems reasonable. However, the shear samples tend to tear progressively from the edge of the notch, in which case the truncation condition is met too early. On the other hand, choosing $n = n_f$ would require physical crack propagation and is not recommended. In the current work, setting $n = 0.25 n_f$ provided a good compromise between the two cases. For both tensile specimen the results are very similar for any $n \in [1, n_f]$ since failure propagates rapidly through the entire cross section.

The optimization results in the parameters given in Tab. 3 and the normalized force-displacement and strain-displacement curves plotted in Fig. 6. The agreement of simulation and experiment is at an acceptable level of accuracy. The strain values are taken in the center of the surface of the calibrated zone. In the experiments they are measured with DIC, for the simulations the strain value of the surface element at the corresponding position is taken. Regarding the ultimate tensile and the 45° shear sample the strain values match very well, while there is a slight offset on the notched tensile test and the strain is underestimated on the 0° shear sample towards the end of the test.

a	b	c
1.29	0.70	0.08

Tab. 3: Parameters of the Hosford-Coulomb model given by Eq. 3.

Considering the range of stress states covered, it is worth mentioning that the first element to fail in each computation does so in the triaxiality range of $\eta \in [1/3, 2/3]$. This is shown in Fig. 7 where the evolution of effective plastic strain and triaxiality is plotted for each element with

respect to the calibrated failure curve. While the elements in the center of the shear samples are loaded in a shear stress state, failure begins from the edge in the notch which is under tension. Despite the first elements failing only under tension, parameter c which acts mainly on the part of the failure curve $\eta < 1/3$ is still found to have an influence on the results since other elements failing later in the computation are subject to such stress states.

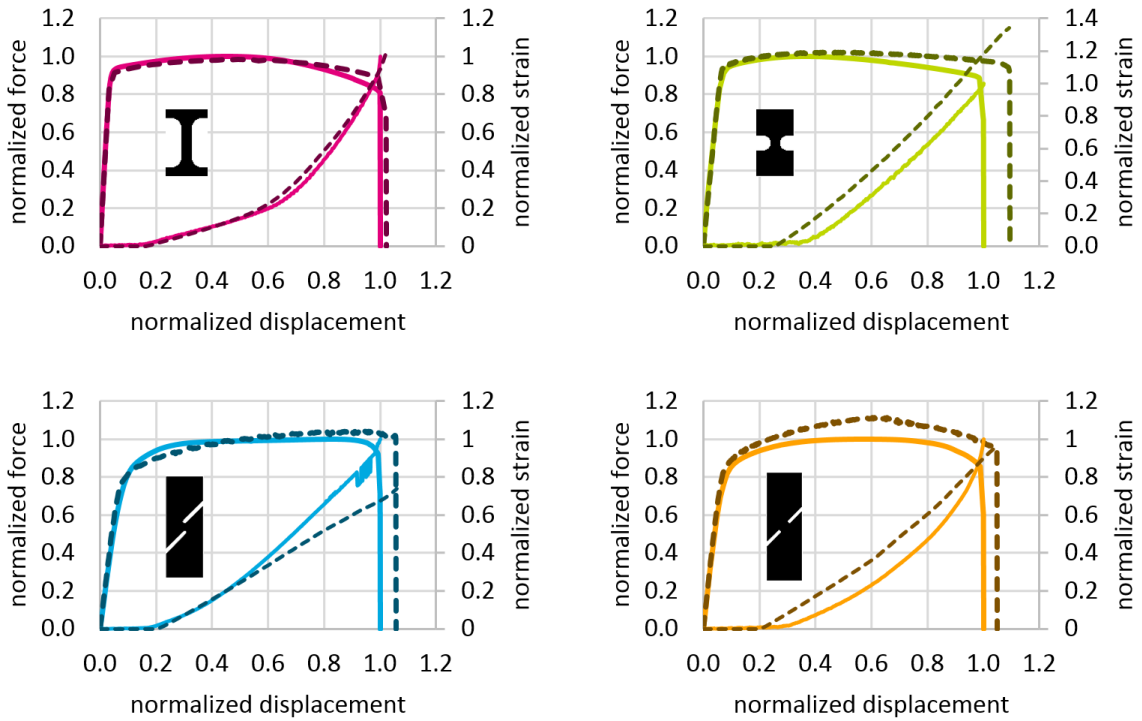


Fig. 6: Normalized force and strain over displacement curves for ultimate tensile, notched tensile, 0° shear, and 45° shear samples, from top left to bottom right. Average values of experiments are plotted as solid lines, the simulation results as dashed lines. The simulation results are truncated after the failure of 25% of all failed elements.

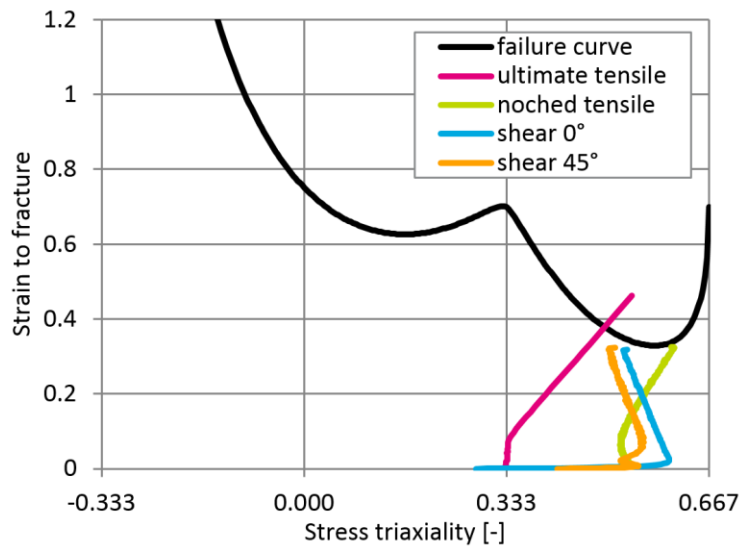


Fig. 7: Strain and triaxiality of the first element to fail in each computation compared to the effective plastic strain to failure curve.

Validation

Using sheets of the same coil as was used for calibration, square profiles are manufactured by bending and friction stir-welding of two symmetrical shells. After sawing the extremities and making a small indentation to initiate buckling at a repeatable location, the profiles are heat-treated and tested in quasi-static axial crush. The width of the square section is 85mm and the total height is 300mm. In order to validate the ability of the previously calibrated material model to predict the fracture, the test is simulated with solid elements; the element width is around 1mm, 5 elements are used through the thickness, and the fully integrated quadratic formulation (ELFORM=3) is chosen. As shown in Fig. 8, the correlation between simulation and experiment on the vertical force is good even if a small shift on the displacement is observed. In addition, a good qualitative agreement is observed on the strain fields presented in Fig. 9 and 10. Concerning the fracture, only some limited cracks are found experimentally on the external face inside the last fold. The extremely good crushability in conjunction with high strength is confirmed. In the computation, element erosion occurs in the same areas which constitutes a good result. A comparison of the crack inside the third fold is detailed in Fig. 10 for the experiment and simulation. Also, the effective total strain measured just above the crack on the underside of the fold is plotted in Fig. 11 for both cases. In terms of the strain value they match well, however the same shift in displacement as was observed for the macroscopic force is present.

A possible reason for the shift in displacement could be found in the fold geometry. The first folds in the experiments are flatter and smaller than in the simulation. This larger fold leads to the higher force value over a longer displacement in the simulation after the initial peak. The following folds in the simulation are seen to initiate about 15mm below their corresponding position in the experiment, which matches the shift of the force and strain curves. A possible reason for this could be the element size limiting the fold radius. Also, the manufacturing of the profile which includes bending by 90° and friction-stir welding was not taking into account, considering initially uniform and undamaged material. Some other open issues remain, like the crack morphology which can only be captured very coarsely or the contact between the newly revealed element faces and edges.

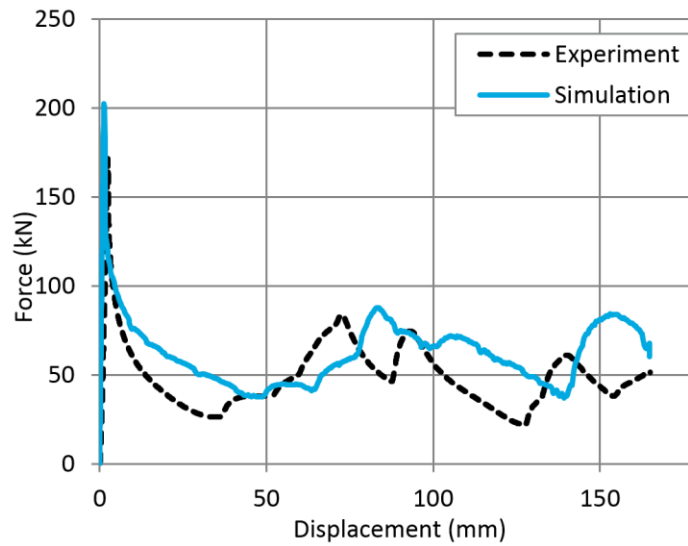


Fig. 8: Comparison of the macroscopic vertical force. The level of force matches well but a small shift in displacement is observed.

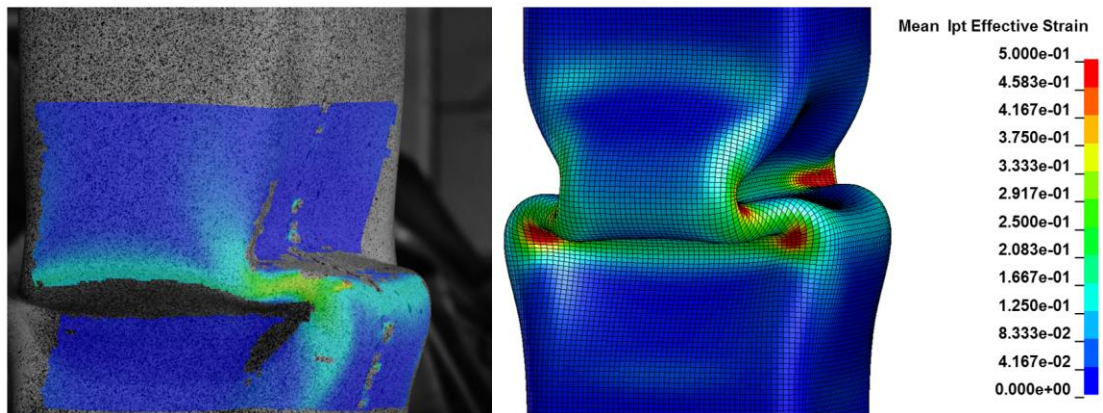


Fig. 9: Comparison of the effective total strain measured by DIC (left) and computed (right) with the same fringe range [0, 0.5] on the first fold.

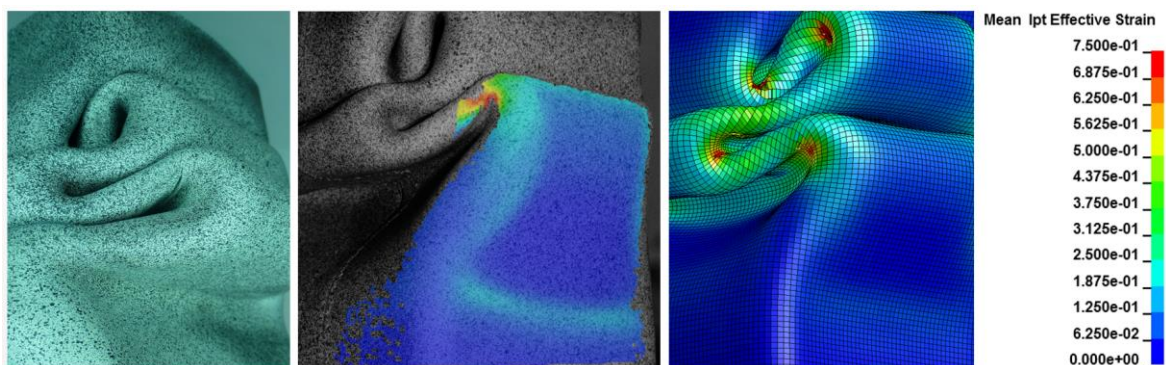


Fig. 10: Post-mortem picture of the crack inside the fourth fold (left), strain field measured by DIC (center) and computed (right) with the same fringe range [0, 0.75].

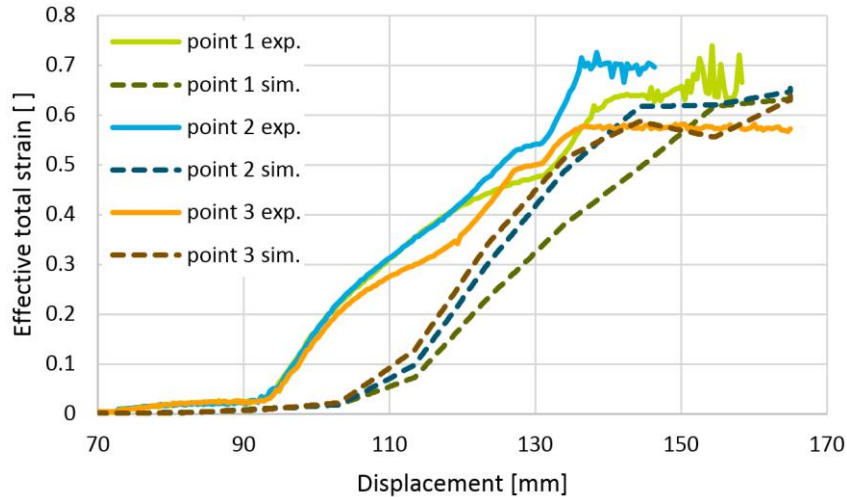


Fig. 11: Comparison of the effective total strain just above the crack in the experiment (solid lines) and simulation (dashed lines). A shift in displacement is observed consistent with the force measurements.

Transfer of Damage Model from Solid to Shell

For the simulation of automotive components, shell elements are the discretization of choice. This means that the damage and fracture model calibrated with solid elements must be transferred to shell elements. Assuming the introduced damage variable is a material property, the model should be directly applicable to shell elements as long as the plane stress assumption is valid. Since this is not the case for the samples used for calibration of the damage model, the simulation of the larger tensile test used for the identification of the flow curve is used for the transfer. This sample has a width of 20mm over the calibrated length of 80mm, which is on the border of validity for the plane stress assumption considering the thickness of 2.5mm.

The result of applying the unaltered damage model calibrated with solid elements to a shell element model with the same element size of 0.1mm edge length is shown in Fig. 12 together with the experimental results. For both element types failure is predicted within the range of the experiments. The shell elements fail earlier since the plane stress assumption is not valid during necking and the shell elements overestimate thinning. This leads to an increase of plastic strain and thus higher damage and earlier failure. However, this effect is considered tolerable judging by the agreement with the experimental results.

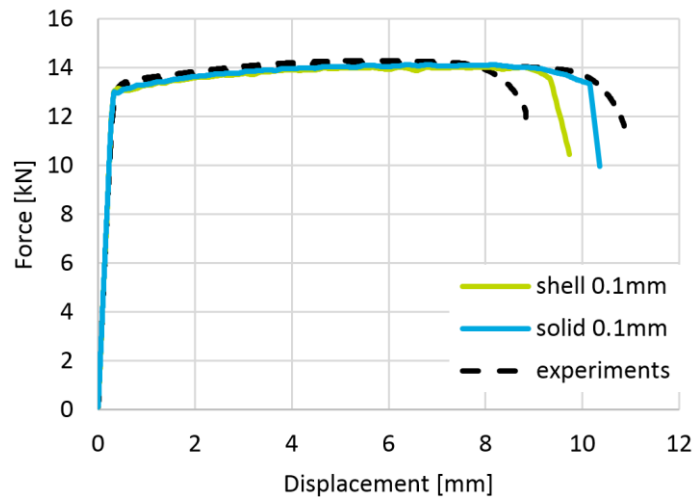


Fig. 12: Transfer of damage model from solid to shell elements

Thus, the damage model can be transferred directly to the shell element models. An element size dependent regularization is calibrated to account for the mesh size effects during necking. The result of the regularization is shown in Fig. 13.

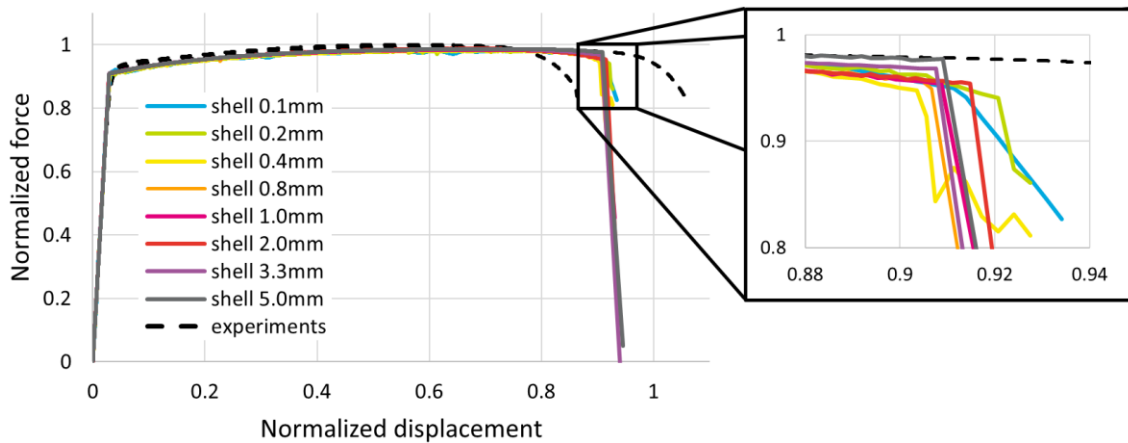


Fig. 13: Element size regularization for shell element meshes

Summary and Outlook

In this work, a failure model for Securalex[®] HS based on the Hosford-Coulomb model is presented. The calibration is done with solid elements due to the size and proportions of the samples used for fracture calibration. Good agreement between the experiments and simulations can be observed for both the macroscopic force-displacement curves and the local strain on the surface of the samples. Using a quasi-static axial crush test, the resulting GISSMO failure card is validated. Since the goal is to create a failure card for shell elements, the influence of the Lode

angle parameter is neglected throughout the calibration process. Despite this simplification, the results of the simulations are in good agreement with the experiments and able to predict failure at the correct locations. Finally, the failure model is applied to shell elements and is shown to deliver reasonable results within the range of the experiments without any further modification.

The next step is to validate the shell model using a macroscopic test like the quasi-static axial crush test used for validation with solid elements. The element size regularization required for this has already been performed. Regarding the calibration process, it is seen that the choice of samples is not optimal, since failure of the first element takes place in similar stress states for all samples. Including different samples in the calibration process, like bending or pure shear, could lead to a more homogeneous distribution of the stress states at failure for calibration. Also, redesigning the sample geometry to have a larger calibrated zone considering the sheet thickness could be considered to use shell elements in the failure calibration process.

References

- [1] T. Wierzbicki and L. Xue: On the effect of the third invariant of the stress deviator on ductile fracture. Technical report, Impact and Crashworthiness Laboratory, Massachusetts Institute of Technology, Cambridge, MA, 2005.
- [2] D. Mohr and S.J. Marcadet: Micromechanically-motivated phenomenological Hosford–Coulomb model for predicting ductile fracture initiation at low stress triaxialities. *International Journal of Solids and Structures* (67-68), 2015.